Title

Nonequilibrium Thermodynamics of Colloidal Gold Nanocrystals Monitored by Ultrafast Electron Diffraction and Optical Scattering Microscopy

Journal

ACS Nano, 14(4)

ISSN

1936-0851

Authors

Guzelturk, Burak
Utterback, James K
Coropceanu, Igor
et al.

Publication Date

2020-04-28

DOI

10.1021/acsnano.0c00673

Peer reviewed

Nonequilibrium Thermodynamics of Colloidal Gold Nanocrystals Monitored by Ultrafast Electron Diffraction and Optical Scattering Microscopy

Burak Guzelturk,* James K. Utterback, Igor Coropceanu, Vladislav Kamysbayev, Eric M. Janke, Marc Zajac, Nuri Yazdani, Benjamin L. Cotts, Suji Park, Aditya Sood, Ming-Fu Lin, Alexander H. Reid, Michael E. Kozina, Xiaozhe Shen, Stephen P. Weathersby, Vanessa Wood, Alberto Salleo, Xijie Wang, Dmitri V. Talapin, Naomi S. Ginsberg, and Aaron M. Lindenberg*

ABSTRACT: Metal nanocrystals exhibit important optoelectronic and photocatalytic functionalities in response to light. These dynamic energy conversion processes have been commonly studied by transient optical probes to date, but an understanding of the atomistic response following photoexcitation has remained elusive. Here, we use femtosecond resolution electron diffraction to investigate transient lattice responses in optically excited colloidal gold nanocrystals, revealing the effects of nanocrystal size and surface ligands on the electron−phonon coupling and thermal relaxation dynamics. First, we uncover a strong size effect on the electron−phonon coupling, which arises from reduced dielectric screening at the nanocrystal surfaces and prevails independent of the optical excitation mechanism (*i.e.*, inter- and intraband). Second, we find that surface ligands act as a tuning parameter for hot carrier cooling. Particularly, gold nanocrystals with thiol-based ligands show significantly slower carrier cooling as compared to amine-based ligands under intraband optical excitation due to electronic coupling at the nanocrystal/ligand interfaces. Finally, we spatiotemporally resolve thermal transport and heat dissipation in photoexcited nanocrystal films by combining electron diffraction with stroboscopic elastic scattering microscopy. Taken together, we resolve the distinct thermal relaxation time scales ranging from 1 ps to 100 ns associated with the multiple interfaces through which heat flows at the nanoscale. Our findings provide insights into optimization of gold nanocrystals and their thin films for photocatalysis and thermoelectric applications.

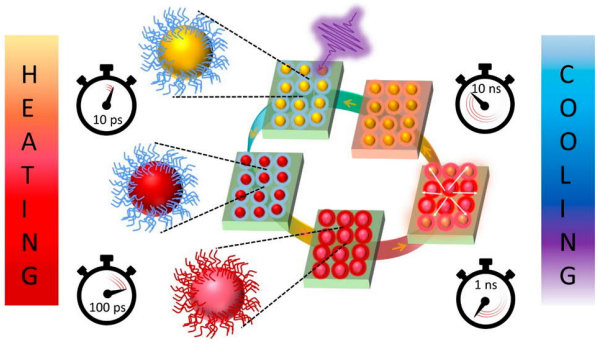

KEYWORDS: *colloidal nanocrystals, electron−phonon coupling, hot carriers, ligands, ultrafast electron diffraction, thermal transport, time-resolved microscopy*

Colloidal gold nanocrystals (NCs) offer favorable properties including strong local electromagnetic field enhancements,[1,2] tunable plasmon resonances,[3] and ease of solution processability,[4,5] which make them appealing for a large set of applications ranging from photocatalysis[6,7] to thermoelectrics[8] and photothermal therapy.[9,10] In these applications, successive energy conversion from light to energetic carriers and then into heat determines key functionalities.[11,12] Therefore, investigation of energy conversion processes in these NCs under nonequilibrium conditions has become an active field of research.[12−14] Prior works have typically employed transient optical probes, *e.g.*, transient reflectivity, to monitor dynamic processes such as hot carrier cooling[15−22] and thermal relaxation.[23−28] Although

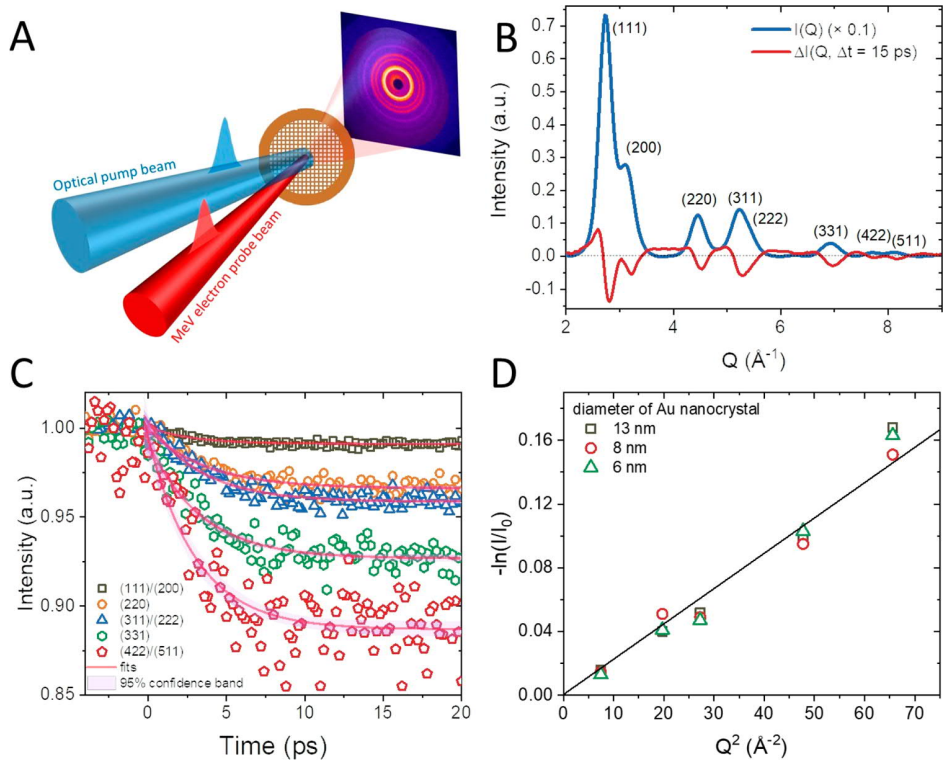

Figure 1. (a) Schematic showing optical pump/ultrafast electron diffraction (UED) probe measurements in a transmission geometry. (b) Static radially integrated diffraction intensity (blue) and transient differential diffraction intensity (red) (Δt = 15 ps) as a function of scattering vector Q in a gold NC sample (diameter: 13 nm, ligand: OAm) (excitation wavelength = 340 nm). Diffraction peaks are marked with their (*hkl*) indices. (c) Time-resolved signals (excitation wavelength = 340 nm) measured at different diffraction peaks showing that the diffraction intensity decreases transiently. (d) $-\ln(I(Q, \Delta t = 15\text{ ps})/I_0)$ is plotted as a function of Q^2 showing a linear scaling, indicating that the transient disordering of the NCs follows the Debye−Waller effect.

transient optical measurements are widely used and well established, they only provide a view based on the electronic structure. As a result, transient signals are convolved together with electronic processes including electron−electron and electron−interface scattering, making the interpretation of the lattice response rather complicated. In contrast, transient atomic structure probing, which can be achieved using pulsed X-ray[29,30] or electron-beam[31−35] sources, provides direct access into the nonequilibrium thermodynamic processes as reflected in the photoinduced structural responses, which have not been studied in colloidal gold NCs before.

Earlier studies using transient optical methods have explored the role of NC size, shape, and surface ligands on carrier cooling in gold NCs,[14,16−18,22,36] which provide important implications for photocatalysis applications. While previous studies[3,15,16,18] indicated no strong dependence of electron−phonon coupling on the NC size, ref 17 showed a strong dependence, which was attributed to an electron spill-out effect[37] and change in dielectric screening at the NC surfaces. Overall, prior reports indicated conflicting findings on the effect of NC size. As noted by a recent review,[13] prior optical measurements, which used regenerative femtosecond lasers, extrapolated experimental lifetimes as a function of fluence to estimate electron−phonon coupling, which was needed since these measurements do not provide a direct proxy of the temperature. However, the extrapolation approach led to uncertainties in the estimates of electron−phonon coupling coefficients. Size inhomogeneities and excitation-induced NC melting and sintering were also other factors behind the observed discrepancies. The role of surface ligands has also been investigated for its effects on carrier cooling[17−19,38] and thermal relaxation.[39,40] Nevertheless, prior reports again did not show a consistent picture of the effects of surface ligands on the electron−phonon coupling. Although ref 17 did not find any effect of the NC's surrounding environment on the electron−phonon coupling, others[18,19] indicated that surface ligands could modify carrier cooling either through vibrational or electronic coupling. Recent theoretical works also proposed that direct and indirect energy transfer processes at the metal/chemical adsorbate interfaces can help for generating longer-lived hot carriers,[20,41−43] but the effects of such energy transfer processes on the electron−phonon coupling have not been understood.

In addition to electron−phonon coupling, thermal relaxation and thermal transport have become a subject of interest in these NCs for biological as well as thermoelectric applications. Prior works mostly focused on gold NCs in liquid environments where the thermal conductance of various NC/solvent interfaces was characterized *via* transient absorption[23,28,44] or time-resolved infrared spectroscopy.[26] On the other hand, little is understood as to how the thermal properties emerging in NC thin films are related to those of NCs dissolved in solvents. A recent study using frequency domain thermal reflectance showed that macroscopic thermal conductivity in thin films of gold NCs is quite poor, arising from a large vibrational impedance mismatch at the NC/ligand interfaces.[39] Overall, prior works highlighted the importance of controlling surface chemistry, morphology, and film packing to tailor thermal

properties in NC thin films.[40,45,46] Nevertheless, dynamical aspects of thermal relaxation and transport in gold NC films at the nanoscale have remained unexplored to date.

In this work, we investigate the nonequilibrium thermodynamic processes occurring in colloidal gold NC thin films measured by femtosecond electron scattering and spatiotemporally resolved optical scattering approaches. Using these, we investigate the effects of NC size, surface ligands, and excitation mechanism on the electron−phonon coupling and thermal relaxation dynamics. Studying NC samples with diameters ranging from 5 to 13 nm (with a standard deviation of 5%), we demonstrate a prominent size effect that results in stronger electron−phonon coupling as the NC size is decreased. This size effect is associated with a change in dielectric screening at the NC surfaces; hence it emerges independent of the excitation mechanism. In the case of surface ligands, we compare NCs having either covalently bonded thiol-based ligands (dodecanethiol (DDT) and ethanedithiol (EDT)) or weakly coordinated amine-based ligands (oleylamine (OAm)). We show that electron−phonon coupling is not affected by the type of ligand when the carriers are excited through interband transitions. On the other hand, we observe a strong modification of the electron−phonon coupling once the carriers are excited by intraband transitions. The ligand effect is related to an electronic coupling of the plasmonic hot carriers at the NC/ligand interfaces. Furthermore, we complement ultrafast electron diffraction measurements with stroboscopic optical scattering microscopy to spatiotemporally monitor both out-of-plane and in-plane thermal transport in the NC films. By virtue of using two different approaches that both measure dynamics at the nanoscale beneath the bulk regime, we reveal the subdiffusive nature of heat transport in gold nanocrystal films and the microscopic physics of heat transfer at the smallest, NC/ligand scales, at which principles such as bulk conductivity begin to lose their meaning. Altogether, we directly characterize the thermal relaxation in films of gold NCs with organic ligands across a broad range of time and length scales arising from the cascaded heat transfer across multiple organic/inorganic (*e.g.*, NC/ligand) interfaces in these composite materials.

RESULTS AND DISCUSSION

Transient Lattice Heating Dynamics Probed by Ultrafast Electron Diffraction. We perform optical pump/ultrafast electron diffraction (UED) probe measurements using the mega-electronvolt ultrafast electron diffraction beamline facility at SLAC.[47] We employ gold NC thin films on ultrathin carbon grids with a submonolayer NC coverage (see Figure S1). Figure 1a depicts the experimental configuration. The optical excitation and the pulsed electron beam are quasi-collinear with respect to each other with the diffraction from the sample measured in a transmission geometry. Figure 1b shows azimuthally integrated diffraction intensity as a function of scattering vector (Q) in the case of a gold NC sample (diameter: 13.4 nm, ligands: OAm). Figure 1b also depicts the transient change in the diffraction intensity ($\Delta I(Q, t)$) measured at a pump−probe delay of Δt = 15 ps. In response to the optical excitation, $\Delta I(Q, \Delta t = 15\ \text{ps})$ exhibits a loss of intensity around the diffraction peaks, while the intensity in between the peaks (diffuse scattering regions) increases. Figure 1c shows $I(Q, t)/I_0$, transient peak intensity normalized by the static intensity, as a function of pump−probe delays recorded at five different diffraction peaks in the same sample (see Methods). Diffraction intensity decreases for all diffraction peaks within the first 10 ps. Also, changes in $I(Q, t)/I_0$ become progressively larger for peaks at higher Q. These observations imply that the NCs become transiently disordered following photoexcitation due to heating of the lattice *via* hot carrier cooling. This transient response can be explained by a Debye−Waller effect,[32,48] which relates the change in diffraction intensity to thermally induced atomic mean square displacements as $I(Q, t)/I_0 \approx \exp\left(-\frac{Q^2\langle u(t)^2\rangle}{3}\right)$, where Q is the scattering vector and $\langle u(t)^2\rangle$ is the time-dependent atomic mean squared displacement. In the Debye−Waller model, the transient intensity has the following dependence: $-\ln(I(Q, t)/I_0) = \frac{Q^2\langle u(t)^2\rangle}{3}$. To check if the response in the gold NCs follows a Debye−Waller model, we plot $-\ln(I(Q, \Delta t = 15\ \text{ps})/I_0)$ as a function of Q^2 for samples with different diameters studied here in Figure 1d (see Figure S2 for other cases). We find that $-\ln(I(Q, t)/I_0)$ is linear as a function of Q^2, consistent with a Debye−Waller effect and indicating the time-resolved diffraction changes track the buildup of the atomic mean square displacements as the energy is transferred from the electronic system to the lattice. We estimate the atomic root-mean-square displacements $\sqrt{\langle u^2(t)\rangle}$ to be ∼0.08 Å for a ∼100 K transient temperature jump in the gold NCs, obtained by applying the Debye−Waller factor in Figure 1d. In addition to the changes in the diffraction peak intensities, the peak positions also change after optical excitation due to a lattice expansion effect arising from the temperature jump[32] in the NC lattice. The diffraction peaks transiently shift toward lower Q, and the magnitude of the shifts is up to 0.1%, consistent with the temperature jumps estimated here (see Figure S4). The peak shifts show oscillations arising from coherent excitation of radial breathing modes whose frequencies are in good agreement with prior reports in similar size NCs.[13]

To gain better insight into the nature of the optically induced disorder, we compare it to its thermally induced counterpart. For this, we perform static electron diffraction measurements as a function of temperature (Figure S3) and calculate the atomic pair distribution function ($G(r)$) as well as the differential atomic pair distribution function ($\Delta G(r)$) (see SI). Figure 2a shows $G(r)$ for a gold NC sample (diameter: 13.4 nm, ligands: OAm) measured at room temperature exhibiting the nearest neighbor correlation peaks all agreeing with a prior report[49] (see green arrows in Figure 2a). Figure 2a also shows $\Delta G(r)$ measured in the same NC both for a static temperature jump (200 K → 300 K; ΔT = 100 K) and under femtosecond optical excitation (λ_{exc} = 510 nm, I_{exc} = 0.8 mJ/cm^2) with pump−probe delays of Δt = 15 ps and Δt < 0 ps. $\Delta G(r)$ induced by both static temperature jump and transient optical excitation (Δt = 15 ps) exhibit the same profile, which shows a broadening of the nearest neighbor correlations (*i.e.*, a decrease at the peak position and increase at the sides) as expected from a temperature jump induced disordering[32] (see Figures S5 and S6 for $\Delta G(r)$ in other NC samples). Therefore, the transient lattice response induced by a femtosecond optical excitation is the same as that induced by a jump in the lattice temperature. In the case of Δt < 0 ps, $\Delta G(r)$ does not show any signal as expected, highlighting the low noise level of this calculation. This analysis overall indicates that we can use the temperature-dependent static electron diffraction measure-

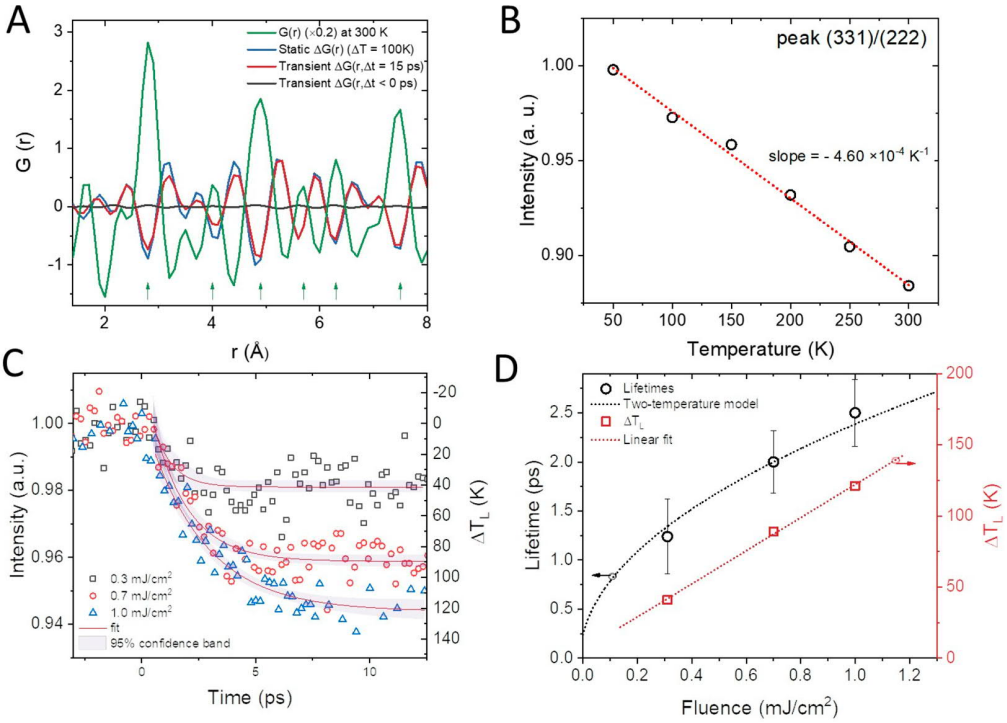

Figure 2. (a) Atomic pair distribution function $G(r)$ (green) measured at room temperature in a gold NC sample (13 nm, OAm). $G(r)$ is scaled by 0.2 for demonstration purposes. Green arrows indicate the positions of the nearest neighbor correlation peaks that are consistent with prior literature. Transient atomic pair distribution function $\Delta G(r)$ is shown for a static temperature jump of 100 K (blue) and transient optical excitation with pump−probe delay of 15 ps (red) and before time zero (black). (b) Diffraction intensity measured at the (311)/(222) peak as a function of temperature. The slope is used to calibrate transient temperature jumps as explained in the main text. (c) Transient response in diffraction peak intensity in a gold NC sample (5.2 nm, DDT) under different excitation fluences when λ_{exc} = 400 nm. Single-exponential fits to the experimental data and 95% confidence intervals are shown. (d) Debye−Waller lifetime (left y-axis) and transient lattice temperature jump ΔT_L (right y-axis) as a function of the excitation fluence. The Debye−Waller lifetimes are modeled based on a two-temperature model explained in the main text.

ments to calibrate the transient temperature jumps in the samples induced by optical excitation.[48,50] Therefore, the UED approach is expected to improve the accuracy of assessing electron−phonon coupling over prior transient optical measurements, which did not have a direct access into transient temperatures in the material. Figure 2b shows static $I(Q)$ recorded at the (311)/(222) peak as a function of sample temperature, where $I(Q)$ is normalized with respect to the lowest temperature. $I(Q)$ shows a linear scaling over a temperature range of 250 K with a slope of -4.6×10^{-4} K^{-1}, which we use in the rest of paper as a calibration coefficient to estimate transient jumps in the lattice temperature of the NC samples. We avoid static heating of the NC samples above 300 K in order to prevent melting and sintering. On the basis of the linearity of the diffraction signal as a function of temperature in Figure 2b, we assume that the same calibration applies for transient lattice temperatures up to ~450 K. The calibration curve measured at another peak, (220) (see Figure S3b), also consistently produces the same lattice temperature jumps as found using the (311)/(222) peak.

Effect of the Excitation Fluence. First, we study the effect of the excitation fluence on the transient lattice dynamics. For this, we excite a gold NC sample (diameter: 5.2 nm, ligands: DDT) at 400 nm with three different fluences (0.3 to 1 mJ/cm^2). Figure 2c shows $I(Q, t)/I_0$ recorded at the (311)/(222) peak. Using the temperature calibration curve, we estimate the transient lattice temperature (ΔT_L) as a function of time (see Figure 2c). We calculate the Debye−Waller lifetime (τ) by fitting a single-exponential decay to the experimental data. Therefore, τ denotes the equilibration time for the energy transfer from hot carriers into the phonon bath of the NC. Figure 2d depicts τ and ΔT_L as a function of excitation fluence. To interpret the experimental results, we use a two-temperature model that is commonly used to analyze nonequilibrium dynamics in metallic systems and provides reasonably good agreement with experiments.[51,52] Two coupled first-order differential equations relate the energy transfer among the hot carriers and the lattice:

$$C_e \frac{dT_e}{dt} = -g(T_e - T_L)$$

$$C_L \frac{dT_L}{dt} = g(T_e - T_L)$$

where C_e and C_L are the volumetric electron and lattice heat capacities, respectively. g is the electron−phonon coupling coefficient, and T_e and T_L are the electron and lattice temperatures, respectively. In metals $C_e = \gamma T_e$, where γ is the heat capacity coefficient. Therefore, the electronic heat capacity depends on the electron temperature (T_e). By solving these coupled equations, we obtain the Debye−Waller lifetime $\tau = \frac{C_e}{g} = \frac{\gamma(\Delta T_e^{max} + T_{RT})}{g}$. This relation is valid under the assumption that $C_e \ll C_L$, which commonly holds since C_L

is more than 2 orders of magnitude larger than C_e when T_e = 300 K,[16] and the maximum T_e never exceeds 3000 K here. T_{RT} is 300 K and ΔT_e^{max} is the initial jump in the transient electron temperature due to optical excitation, which is reached within 50−100 fs after initial thermalization *via* electron−electron scattering.[13,53] The transient jump in the lattice temperature is denoted ΔT_L, which is equal to $\frac{1}{2}\frac{\gamma((\Delta T_e^{max}+T_{RT})^2-(T_{RT})^2)}{C_L}=\frac{U}{C_L}$, where U is the absorbed energy per unit volume.

Figure 2d shows that the experimental ΔT_L scales linearly with the excitation fluence and extrapolates to 0 when the excitation fluence is off. This indicates that we are in a linear response regime in terms of absorption strength. In the case of Debye−Waller lifetimes, we make use of the two-temperature model where $\tau=\frac{\gamma(\Delta T_e^{max}+300K)}{g}$. We take the bulk gold value of γ = 67.6 J/m^3 K^2 and estimate ΔT_e^{max} from the absorbed energy density (see SI for the calculation). The best fit with the experimental data is achieved when $g \approx 8.5\times10^4 \pm 2.1\times10^4$ J m^{-3} ps^{-1} K^{-1}. The estimated g is independent of the fluence, indicating that g does not depend strongly on the temperature. The electron−phonon coupling coefficient in this NC (diameter: 5.2 nm) exceeds prior reports of g in bulk gold films,[16,51] which is typically $(3.5–4)\times10^4$ J m^{-3} ps^{-1} K^{-1}. This observation points out a strong size dependence of the electron−phonon coupling in gold NCs, which will be discussed in detail in the following section.

Effect of Nanocrystal Size, Ligands, and Excitation Mechanism on the Electron−Phonon Coupling. After establishing that ultrafast electron diffraction provides direct access into the transient lattice dynamics, we investigate the effects of nanocrystal size, surface ligands, and excitation mechanism. For the size effect, we study three different gold NCs with diameters of 13.4, 7.7, and 5.7 nm, all having the same OAm ligands (see Figure S1 for the TEM images). These samples exhibit quite uniform size distributions (σ < 5%), which is required for achieving high-fidelity results on the size effects. For brevity, these NCs are here denoted as 13, 8, and 6 nm in Figure 3. For the ligand effect, we study three different ligands while using an NC sample with the same diameter, *i.e.*, 5.7 nm. We use either amine-based long-chain OAm ligands or thiol-based long-chain DDT and short-chain EDT ligands. DDT and EDT ligands with a thiol-based anchor exhibit strong covalent binding to the gold surface, while an OAm ligand with an amine-based anchor exhibits only a weak and labile coordination to the NC surface.[54,55] Furthermore, we excite all the NCs separately at 340 and 510 nm to study the effect of the excitation mechanism. Photons at 3.6 eV (λ_{exc} = 340 nm) dominantly excite transitions across d to s bands (see Figure S12); hence this excitation scheme is denoted as an interband excitation.[37] On the other hand, photons at 2.4 eV (λ_{exc} = 510 nm) are almost in resonance with the localized surface plasmon energy. Therefore, 2.4 eV photons can excite carriers within the s-band, which is denoted here as an intraband excitation. Nevertheless, 2.4 eV is slightly above the interband excitation onset in gold (2.3 eV[56]); thus, 2.4 eV would also coproduce interband excitations in addition to intraband ones. Although it is not straightforward to estimate the individual contributions of inter- and intraband under 2.4 eV excitation, we expect the dominant channel to be the intraband excitation (see Figure S12).[57]

We show the decay curves in all NC samples recorded at the diffraction peaks in Figures S8 and S9. The Debye−Waller lifetimes (τ) are fitted using single-exponential decays. τ does not change considerably among the fits of different diffraction peaks measured within the same sample (see Figures S7, S10, and S11). Therefore, we average τ fitted for all diffraction peaks in each sample to improve the signal-to-noise ratio in this analysis. Figure 3a and b show τ in different NC samples while exciting at 340 nm (interband) and 510 nm (dominantly intraband), respectively. The pump fluence is kept constant within the linear response region at 1 and 0.8 mJ/cm^2 for the 340 and 510 nm excitations, respectively. Transmission electron microscopy images showed no change in the shape and morphology of the NCs after the UED experiments. Therefore, we avoid irreversible melting/fusion of the NCs[58] and keep them intact during the experiments.

We investigate the effect of the NC size on the electron−phonon coupling. At both excitation conditions, we observe that smaller NCs consistently exhibit shorter τ (Figure 3a,b). This implies that hot carrier cooling strongly speeds up in the smaller NCs. To estimate g as a function of NC size, first we estimate the electronic temperature jump ΔT_e^{max} for all samples. To do this, we calculate the absorbed energy density $U = \Delta T_L \times C_L$ either using the experimental ΔT_L in Figure 3c or by considering the optical extinction coefficients of the gold NCs and the exerted pump fluences (see SI). Both estimates of U (Table S1) are in close agreement, meaning that experimental ΔT_L (Figure 3c) agrees well with the temperature jumps estimated from the absorption cross-section of the nanocrystals and the excitation fluence (see SI). Here we use values for U that are calculated from the experimental ΔT_L to avoid uncertainties associated with the optical extinction coefficients of the different sized NCs used here. Using the calculated U and assuming that the volumetric heat capacity of the NCs is the same as for bulk gold ($C_L = 2.49\times10^6$ Jm^{-3} K^{-1}), we calculate ΔT_e^{max} (see Tables S1 and S2) as ∼2300 K ± 100 K and ∼2500 K ± 100 K under the 340 and 510 nm excitation conditions, respectively. Then, we calculate $g=\frac{\gamma(\Delta T_e^{max}+300)}{\tau}$ in all NC samples under investigation here (see Figure 3d). Figure 3d also indicates $g = 3.85\times10^4$ J m^{-3} ps^{-1} K^{-1} in bulk gold, which is estimated from an earlier UED experiment[59] measuring polycrystalline bulk gold films, also in good agreement with prior reports of g in bulk gold.[16] Figure 3d shows that g strongly increases as the NC size is decreased, which happens independent of the excitation mechanism. The g for the 6 nm gold NC sample is larger by a factor of 2 than the g for bulk gold.

There have been prior contradictory results on the size dependence of electron−phonon coupling in gold NCs. Arbouet *et al.* have predicted a strong size dependence due to decreased dielectric screening at NC surfaces associated with an electron spill-out effect.[17] Because of the spill-out effect, carrier screening at the metal NC surface decreases, which in turn increases the coupling of the carriers to the ions and effectively enhances the electron−phonon coupling (see Figure S13). Here, we apply the dielectric screening model (see SI) proposed in ref 17 to our experimental data. Figure 3e compares the modeled g as a function of the NC size together with the experimental g, demonstrating a very close agreement between the model and the experiment. The agreement is better for the experimental g measured under interband excitation. This observation can be explained by the varying degree of dielectric screening under different excitation conditions. While the intraband excitations within the s-band

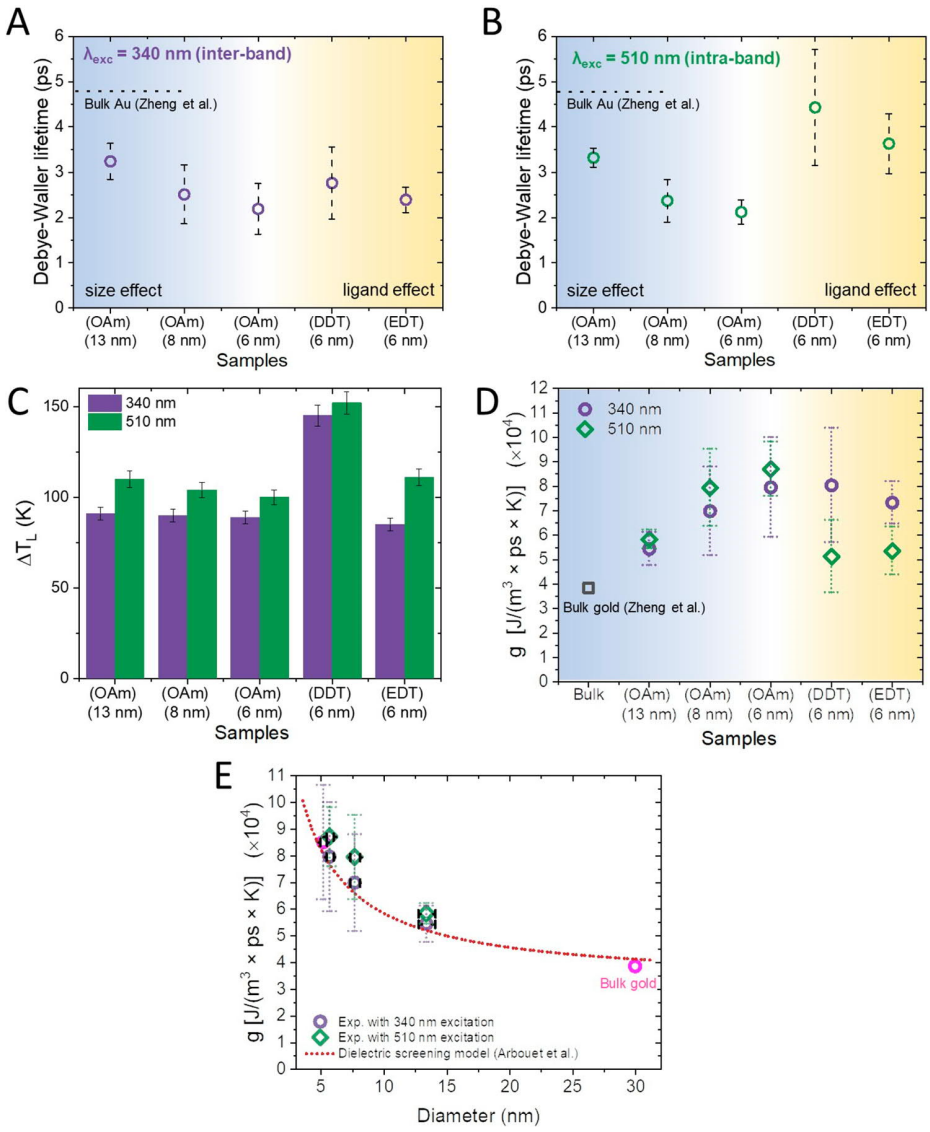

Figure 3. Debye–Waller lifetimes in the gold NC samples with different size and ligands under (a) 340 nm and (b) 510 nm excitation. Samples are labeled by (ligand) on the top and (diameter) at the bottom in the X-axis. (c) Transient jump in the lattice temperature ΔT_L in size and ligand series samples under both excitation conditions. (d) Electron–phonon coupling coefficient (g) in all samples under 340 and 510 nm excitation. g in bulk gold is estimated from a prior report.[59] (e) Experimentally estimated g (circles or squares) as a function of the NC size and calculated g from a dielectric screening model[17] (dashed line). Purple circles for λ_{exc} = 340 nm; pink circle for λ_{exc} = 400 nm; green squares for λ_{exc} = 510 nm. Error bars in g are estimated based on the propagation of the experimental errors in τ and ΔT_L as well as the polydispersity of the particle size.

produce carriers that are highly delocalized at the NC surfaces,[37] interband excitations across the d–s bands produce carriers that are relatively more localized.[37,60] Therefore, a weaker screening is experienced by the carriers generated by the intraband excitations, while the screening is relatively stronger for the interband excited carriers. As a result, g should be larger for the carriers generated by intraband excitation, consistent with the experiment (Figure 3e). For this reason, interband excited hot carriers are longer lived than that of intraband excited hot carriers in the gold NCs with OAm ligands. This finding supports a recent experimental work that showed an enhanced photocatalysis performance under interband excitations as compared to intraband ones in the gold NCs with the amine-based ligands.[57] In addition, another important implication of the size effect is the fact that hot carrier cooling becomes much faster in smaller NCs. Previously, theoretical studies predicted that plasmonic hot carrier generation would be more efficient in the smaller NCs due to their larger surface to volume ratios.[20] However, our finding indicates that increased electron–phonon coupling in the smaller NC acts antagonistically to the hot carrier generation efficiency, which is important to consider for photocatalytic applications.

The NC size is not the only means to modify electron–phonon coupling in the gold NCs. We find that surface chemistry also provides a way to tune hot carrier dynamics. Figure 3a,b show the Debye–Waller lifetimes in the same size gold NC (diameter: 5.7 nm) with three different ligands: OAm, DDT, and EDT. We find that the effect of the ligands is highly sensitive to the excitation wavelength, hence the optical

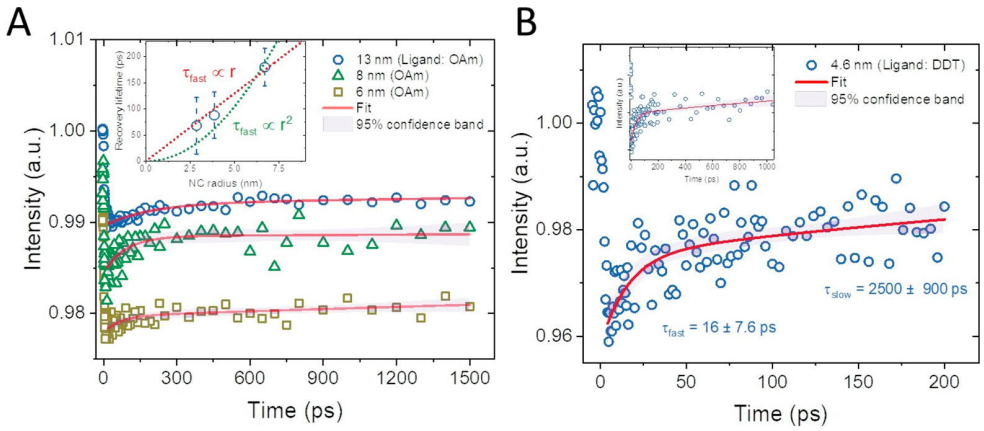

Figure 4. (a) Transient response in the diffraction peak intensity in gold NC samples (diameters: 13.4, 7.7, and 5.7 nm all with OAm ligands) under 510 nm excitation with a fluence of 0.8 mJ/cm^2. Experimental data are shifted in the vertical direction for the 8 and 6 nm samples for demonstration purposes. The inset shows the initial recovery lifetime that scales linearly with the NC radius. (b) Transient response in the diffraction peak intensity in a gold NC sample (diameter: 4.6 nm, DDT ligand). Fast (16 ps) and slow (2.5 ns) time constants were fitted with double-exponential decay. The inset shows the transient response in the same sample over a longer pump−probe delay window.

excitation processes. In the case of interband excitation, we only observe a weak effect associated with different ligands (Figure 3a). On the other hand, under 510 nm (dominantly intraband), nanocrystals with the thiol-based ligands exhibit a slower lattice heating response as compared to the one with an amine-based ligand (Figure 3b) while the lattice temperature jumps are roughly equivalent (*e.g.*, OAm *vs* EDT in Figure 3c). Figure 3d shows the experimentally estimated g in these samples with different ligands. Under interband excitation (λ_{exc} = 340 nm), we find that g is *ca.* $8 \times 10^4 \pm 1.6 \times 10^4$ J m^{-3} ps^{-1} K^{-1} for the samples with three different ligands. However, under intraband excitation (λ_{exc} = 510 nm) g is $5.0 \times 10^4 \pm 1.4 \times 10^4$ J m^{-3} ps^{-1} K^{-1} for the samples with thiol-based ligands (DDT and EDT) and g is much larger ($8.7 \times 10^4 \pm 1.2 \times 10^4$ J m^{-3} ps^{-1} K^{-1}) for the sample with an OAm ligand. These observations indicate that the ligand makes a difference in the hot carrier cooling dynamics, especially for the carriers that are generated by intraband excitations. As discussed above, intraband-generated carriers are highly delocalized; hence they can interact more with the nanocrystal surfaces. In this respect, we explain the effective suppression of the electron−phonon coupling when using thiol-based ligands due to the coupling of the delocalized surface hot carriers[61,62] with the electronic states of the ligand molecules. Previously, chemical interface damping,[41,63] a term used to describe broadening of the surface plasmon peaks, has been observed in the gold NCs with thiol-based ligands as attributed to the enhancement of electron/interface scattering at the nanocrystal surfaces.[63] Here, we hypothesize that surface hot carriers can sample the electronic states of the DDT and EDT ligands outside the nanocrystal, and, as a result, cooling of the hot carriers can be delayed and the electron−phonon coupling becomes effectively weaker. Transient lattice temperature jumps (Figure 3d) do not change when using thiol-based ligands as compared to an amine-based one, which implies that the main hot carrier relaxation still happens in the nanocrystal and the surface hot carriers do not couple strongly to the vibrations of the ligand molecules as alluded to by recent reports.[43,64,65] In addition, the suppression of the electron−phonon coupling is comparable in the nanocrystals with DDT and EDT ligands, although EDT has a much shorter alkyl chain than that of DDT. This indicates that the binding group of the ligand is more important to the ligand effect observed here. Overall, short alkyl chain ligands with thiol-based anchor groups, as in the case of EDT, can synergistically increase plasmonically generated hot carrier lifetimes while allowing for efficient photoinduced charge transfer at the nanocrystal surfaces for hot carrier utilization[66] in photocatalysis applications. Our results indicate that tailoring surface chemistry in metallic NCs can enable longer lived hot carriers, and engineering of the NC surfaces can help further slow down hot carrier cooling desired for photocatalysis.[64,67]

Thermal Relaxation and Transport in Gold Nanocrystal Films. Next, we investigate thermal relaxation and transport in gold NC films by resolving the recovery dynamics of the transient lattice responses. Figure 4a shows the Debye−Waller effect recovering in the NC samples that have the same ligand (OAm) with different diameters over a 1.5 ns pump−probe delay time window. We find that recovery dynamics exhibit an initial fast time constant (τ_{fast}), which is 68 (±54) ps, 88 (±44) ps, and 180 (±36) ps for the NCs with diameters of 5.7, 7.7, and 13.4 nm, respectively. We hypothesize that this initial recovery time arises from the heat transfer from the NC cores into the surrounding ligands, which is expected to be the first step of thermal relaxation in these NCs. To test this hypothesis, we consider potential cooling modes in metal NCs[23] that can take place through either thermal effusivity of the surrounding (*e.g.*, NCs dissolved in solvents) or interfacial heat transfer at the NC/adsorbate interfaces. The thermal relaxation lifetime (τ_{relax}) has been shown to have a different scaling as a function of the NC radius (r) in these two different cases.[23] $\tau_{relax} \propto r^2$ in the case of cooling *via* thermal effusivity, while $\tau_{relax} \propto r$ in the case of cooling *via* interfacial thermal conductance, where r is the particle radius. In the samples with different NC sizes, we observe that the initial fast recovery lifetime fits better to a linear dependence on the NC radius than a quadratic dependence (see the inset of Figure 4a). This alludes that the initial cooling response in these NCs is due to an interfacial heat transfer process. In this case of interfacial thermal relaxation, $\tau_{relax} = \frac{rC_L}{3G_{int}}$ where G_{int} is the interfacial thermal conductance (NC/ligand) and C_L is the volumetric heat capacity of the NC. We estimate G_{int} to be ~40 ± 8 MW/m^2 K for the gold NC−OAm ligand interface, which is roughly

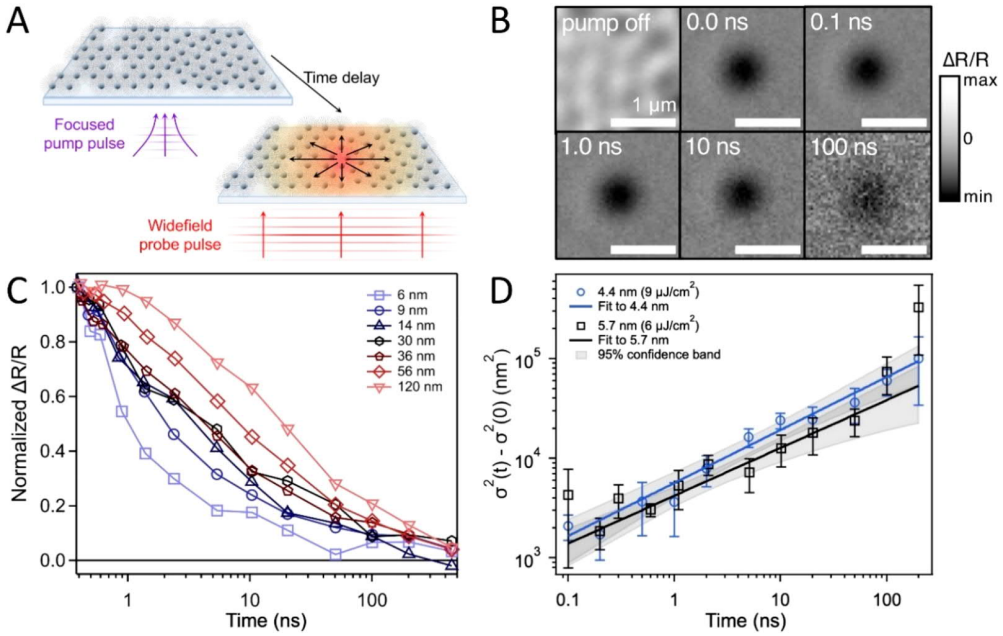

Figure 5. (a) Schematic of the stroboSCAT experiment, in which the sample is excited with a focused pump light pulse and then the subsequent heat diffusion is imaged using a wide-field probe pulse after some time delay. (b) Representative ground-state scattering image (pump off) and stroboSCAT time series on a 100 nm thick region of a film of 4.4 nm gold NCs with DDT ligands. (c) Decay traces of spatially integrated stroboSCAT signal amplitude after excitation with a pump fluence of 9 μJ/cm^2 for different film thicknesses of a 4.4 nm gold NC film on a logarithmic time axis, normalized to unity at ~300 ps. (d) Log–log plot of the mean-squared expansion of the stroboSCAT spatial distributions as a function of time for films of 4.4 and 5.7 nm gold NCs capped with DDT ligands, averaged over five measurements at different positions with the films.

independent of the NC size. This interfacial thermal conductance is comparable to that of NC/organic solvent, *e.g.*, hexane,[25] interfaces where there is no strong chemical bonding, as in the case for the OAm ligand. In the case of strongly coordinating thiol-based ligands (*i.e.*, DDT), we find that the initial thermal relaxation time is much faster (τ_{fast} = 16 ± 7.6 ps) for an NC with a diameter of 5.2 nm (see Figure 4b). Under the interfacial thermal conductance assumption, we estimate G_{int} to be 120 ± 55 MW/m^2 K for the NC/DDT interface, which is 3-fold larger than that of the NC/OAm interface. This observation is consistent with a prior prediction based on molecular dynamics simulations,[68,69] where ref 68 indicated that the interfacial thermal conductance would be enhanced for ligands such as DDT that exhibit stronger vibrational coupling to the NCs. Our estimate of G_{int} for the NC/DDT interface is smaller than the calculated G_{int} in ref 68 by a factor of ~2. We believe that this difference could arise from smaller effective surface coverage of the ligands in our samples as well as surface imperfections.[69] Overall, our observations show that UED directly uncovers the early steps of thermal relaxation dynamics in colloidal NCs and confirms prior theoretical predictions on the enhancement of interfacial thermal conductance across NC/ligand interfaces when using ligands with better vibrational impedance matching with the gold NC itself.[68]

The UED signal also exhibits a slower, nanosecond relaxation time scale (τ_{slow}) that is not fully resolved within the experimental time window (Figure 4b inset). However, complete thermal relaxation cannot be captured with the UED alone due to its limited pump–probe delay times (~few ns). Moreover, spatial aspects of heat transport become increasingly important on these time scales. Thus, we turn to spatiotemporal measurements of heat flow to investigate these behaviors. Specifically, we use stroboSCAT microscopy to monitor thermal relaxation on the nanosecond time scale as well as to spatially probe the nature of in-plane and out-of-plane thermal transport in the gold NC films. stroboSCAT is a recently developed time-resolved interferometric optical scattering microscopy that tracks both electronic and thermal energy flow at the nanoscale.[70] For example, this technique has been used to monitor spatiotemporal charge carrier and heat transport in silicon.[70]

stroboSCAT measures transient changes to a material's local electric polarizability induced by a focused ultrafast pump laser pulse (Figure 5a).[70] These changes are measured by interferometrically detecting the light scattered from the sample, after probing it in wide field, on a CMOS detector and subtracting an analogous image taken in the absence of a pump pulse (Figure 5a,b). In the gold NC films, the resulting differential image contrast maps the spatial distribution of heat in the sample, as reflected by the transient change of scattering cross-section of the NCs, and its evolution as a function of time is directly imaged by the wide-field probe. We report the signal as $\Delta R(r, t)/R$ since the experiment is performed in a reflection geometry, where the scattered light is detected at the field level *via* interference with light reflected from the substrate–sample interface (Figure 5a).[70] Here we use a 405 nm pump light pulse (~100 ps), focused to a spot size of 590 nm (fwhm), to promote interband photoexcitation in films of either 4.4 or 5.7 nm gold NCs with DDT ligands, and a 635 nm wide-field probe light pulse (~100 ps) to visualize the time-dependent scattering profile of the resulting heat distribution, which in this case appears as negative (dark) contrast (Figure 5b). NC films were prepared in a similar

manner to the protocol for the films used for UED experiments, apart from the substrate for stroboSCAT being a glass coverslip; thus, we expect the thermal dynamics observed in stroboSCAT to reflect the nanosecond-scale behavior observed in the UED.

While we will shortly return to the utility of stroboSCAT's spatial resolution, we first examine the decay of the stroboSCAT signal over the ∼300 ps to 450 ns time window to compare decay lifetime components in the time window for which stroboSCAT and UED overlap. Figure 5c shows the decay traces of the spatially integrated signal amplitude for a range of film thicknesses, as determined *via* correlative atomic force microscopy (AFM) (Figure S15). The decay traces exhibit a broad range of time scales, with half-lives that increase with increasing film thickness from 1 ns at 6 nm (monolayer) to 15 ns at 100 nm (∼10 layers) (Figure S16). We attribute this strong change in the signal decay in the nanosecond time window as a function of sample thickness to the thermal dissipation from the NC film to the substrate. The pump attenuation length is >100 nm; hence heat diffusion toward the substrate interface takes longer in thicker films, consistent with the experimental observations. The 1−2 ns half-life of the stroboSCAT decay in monolayer and bilayer regions of the sample (Figure 5c) resembles the slowest, ∼2 ns time scale seen in UED (Figure 4b), which investigated regions of films that consisted primarily of monolayers and bilayers (Figure S1). Therefore, we hypothesize that the nanosecond decay component observed in the UED is also mainly due to thermal dissipation to the substrate. Diffusion within the films should be similar in UED and stroboSCAT because the films were prepared in a similar manner. Moreover, we expect the interfacial heat transfer to occur with similar time scales because the glass substrate used in stroboSCAT and the graphitic carbon substrate of the TEM grid used in UED have similar specific heat capacities.[71,72]

By fitting the spatial distribution of the transient scattering profile to a Gaussian function over time, we monitor heat diffusion with a few tens of nm sensitivity and on time scales from ∼300 ps to 200 ns. Figure 5d shows the in-plane mean-squared expansion of the distributions as a function of time in films of both 4.4 and 5.7 nm gold NCs with DDT ligands, plotted as $\sigma^2(t) - \sigma^2(0)$. The mean-squared displacement curves for the 4.4 and 5.7 nm NC films agree within error, which is consistent with a previous demonstration that macroscopic thermal conductivity exhibits a relatively weak size dependence in such NC arrays.[39] The associated root-mean-squared displacements over the experimental time window are 40−300 nm, corresponding to heat transport over distances much greater than the size of individual NCs. The data in Figure 5d were fit to $\sigma^2(t) - \sigma^2(0) \propto t^{\alpha}$, yielding α = 0.53 ± 0.04 and 0.48 ± 0.09, for the 4.4 and 5.7 nm NC films, respectively. The values of $\alpha < 1$ indicate subdiffusive behavior in both films. The subdiffusive transport is likely due to disordered packing of the NCs in the film.[73,74] This picture is supported by the transmission electron microscope (TEM) images of films prepared in a similar fashion to those measured by stroboSCAT (Figures S1 and S14). By accessing the time rate of change of the mean squared expansion of the photoinduced heat distribution with these spatiotemporally resolved measurements and revealing the subdiffusive evolution, we indicate that the thermal conductivity in these NC films is a time-dependent quantity. Therefore, we suggest that macroscopic measurements of steady state thermal conductivity in disordered NC/ligand composite films should be treated with care. In subdiffusive systems, the apparent diffusivity or conductivity depend on the length and time scale of the measurement.[73,74] In particular, heat transfer occurs with the highest conductance at the NC/ligand interface on sub-100 ps time scales, and the observed conductance for subsequent steps in the cascade decreases progressively as additional heterogeneities are encountered over inter-NC and film/substrate interface length scales. Were one to reduce our detailed mean squared expansion time dependence to the simplest, diffusive case to extract a simple conductance, it would agree with the prior bulk measurement of thermal conductivity in gold NC films performed in ref 39 (Figure S17). With the confidence of this connection, we are able to establish the nature of transport characteristics consistent with, yet at a higher degree of detail than in bulk, ∼μs-scale measurements: we find *via* UED that shorter length scale processes, such as NC/ligand energy transfer, occur at rates that we can corroborate with calculations of material parameters, whereas the tortuosity introduced through the films' spatial disorder on the multi-NC scale slows transport relative to what a calculation using an ordered array of NCs would predict.

CONCLUSIONS

By complementing ultrafast electron diffraction and stroboSCAT we have probed the generation, transport, and dissipation of heat over a broad range of length and time scales in films of gold NCs, revealing the cascaded energy transfer of lattice heating and subsequent heat transfer from the NCs to the ligands, between neighboring NCs, and finally to the substrate. Multiscale studies like the one we have presented provide a more comprehensive way to relate the dynamics observed on nano- and microscales than is typically achieved using a single measurement modality. Such studies often pose new challenges since consistently stitching together information over large dynamic ranges in time and space is itself difficult. UED proves to be extremely useful to extract electron−phonon coupling strength through directly accessed transient lattice heating responses. We reveal the effects of two important properties: the nanocrystal size and its surface ligands. The smaller size (<10 nm) leads to a significantly faster hot carrier cooling due to a decrease in dielectric screening at the nanocrystal surfaces, and this prevails for both inter- and intraband optical excitation conditions. Surface ligands show surprisingly strong modification of the hot carrier cooling rates due to electronic coupling between the plasmonically induced surface hot carriers and the ligands' electronic states. These findings provide guidance toward efficient photocatalysis based on metallic nanomaterials. Particularly, we show that smaller gold NCs (<10 nm) with short thiol-based ligands (*e.g.*, EDT) can combine enhanced hot carrier generation efficiencies[20] with longer lived hot carrier lifetimes; hence these NCs can provide enhanced photocatalytic performances. In the case of thermal transport and recovery, we uncover the spatiotemporal dynamics and interfacial thermal conductances within gold nanocrystal films. We show that thermal relaxation takes place *via* a cascade of thermal relaxation steps with thermal conductances getting consecutively smaller over time. Although thiol-based ligands enhance the interfacial thermal conductance by a factor of 3 as compared to amine-based ones, the overall thermal conductance of the nanocrystal thin films is limited by slower in-plane heat transfer between nanocrystals

as well as out-of-plane heat transfer into the substrate. These findings provide key insights on the thermal management of these colloidal nanocrystals important for thermoelectric and optoelectronic applications.

METHODS

Ultrafast Electron Diffraction and Analysis of Transient Diffraction Peak Intensities. The UED configuration is schematically shown in Figure 1a, and details of the system have been described in a previous report.[47] As the laser source, a multipass-amplified Ti:sapphire laser (800 nm, 60 fs, 360 Hz) was used. Its output is split into two paths. One of the paths is frequency tripled to generate electron beam pulses, which are accelerated to 3.7 MeV (~150 fs in full-width at half-maximum) for 30−40 fC per pulse. The other part of the 800 nm beam is supplied into an optical parametric amplifier to generate either 340 or 510 nm optical pump beams. The size of the electron probe beam was about 100 μm, while the optical pump beam size was ~500 μm. The diffracted electrons were detected by a red phosphor screen and captured using an electron-multiplying charge-coupled device. Time zero for the pump−probe delay is calibrated using a thin single-crystal silicon or bismuth showing a sub-ps sharp signal in time. The delay between the pump and probe pulses was controlled by a translational stage.

We analyzed the diffraction peak intensities similar to our previous work.[32] We first performed radial integration of the diffraction images to get $I(Q)$. Then, we sorted the images by their labels of pump−probe delays. With this, we got $I(Q, t)$. Using either single or double Gaussian fits, we fitted the peak intensity as well as the peak positions for five different diffraction peaks labeled in Figure 1b. Then, we plot $I(Q, t)/I_0$, where I_0 is the intensity of the peaks in the absence of pump beam.

StroboSCAT Measurements. The experimental setup for stroboSCAT measurements has been previously described in detail.[70] Briefly, two laser diodes were used for the pump (LDH-D-C-405, PicoQuant) and the probe (LDH-D-C-640, PicoQuant) with center wavelengths of 405 and 635 nm, respectively, which were controlled by a laser driver (PDL 828-S "SEPIA II" equipped with two SLM 828 driver modules and a SOM 828-D oscillator, PicoQuant). We used a laser repetition rate of 2 MHz, with the pump modulated at 660 Hz, while the pump−probe delay times were controlled electronically using the driver with 20 ps resolution. Both pump and probe were spatially filtered through 25 μm pinholes. The pump beam was telescoped to a ~6 mm diameter, while the probe beam was telescoped to 1 mm and focused into the back focal plane of the objective of a home-built microscope using an f = 300 mm wide-field lens. The two beams were combined using a long-pass filter (DMLP505, Thorlabs), and a 50/50 beamsplitter reflected both beams into a high numerical aperture (1.4 NA) oil-immersion objective (Leica HC PL APO 63×/1.40 NA) and onto the sample, resulting in an overlapped confocal pump and wide-field probe illumination, respectively. Probe light reflected from the sample−substrate interface as well as scattered from the sample are collected through the same objective; the probe light is isolated with a long-pass filter (FEL550, Thorlabs) and focused onto a charged metal oxide semiconductor (CMOS) detector with 5.86 μm square pixels triggered at 660 Hz (PixeLINK PL-D752, equipped with a Sony IMX 174 global shutter sensor) using an f = 500 mm lens placed one tube length (200 mm) away from the back focal plane of the objective. The total magnification is 63 × 500/200 = 157.5, giving 37.2 nm/pixel. stroboSCAT images are generated by taking the difference between pump-on and pump-off raw pixel intensities, normalized to the raw pump-off intensities, yielding $\Delta R/R$ contrast images. Averaged pump-off images are simultaneously recorded at each time delay. Setup automation and data acquisition are implemented in LabVIEW 2014 64-bit. Data analysis and plotting is performed using a combination of imageJ (Fiji),[75,76] MATLAB, and Igor Pro. The pump powers were chosen to be in a regime where the spatially integrated signal decay was independent of pump power.

Sample Preparation. A series of spherical gold nanocrystals with an average diameter ranging from 4 to 13 nm was prepared based on a previously described protocol[77] with oleylamine as the native ligand. The particles were gently precipitated using ethanol and then redispersed in toluene at a concentration of 20 mg/mL. Ligand exchange to DDT was performed by adding an excess of DDT to this solution followed by stirring for 15 min at room temperature. The gold nanocrystals were then precipitated with ethanol and redispersed in toluene. Ligand exchange to EDT was carried out by applying a solid film ligand exchange procedure to films deposited using OAm-capped particles. Briefly, after the initial film was dried, the substrate was immersed in a 2% solution of EDT/IPA for 1 min and then rinsed with IPA. Films used for UED were deposited by placing a 10 μL drop of a 20 mg/mL solution of gold nanocrystals in toluene and allowing it to dry at 1 atm. Films used for stroboSCAT were deposited by placing a 10 μL drop of 10 mg/mL solution of gold nanocrystals in toluene on a 24 × 50 mm VWR #1.5 glass coverslip and allowing it to dry at 1 atm. Glass substrates were cleaned by 10 min sonication in acetone, followed by 10 min sonication in isopropyl alcohol, then immediately dried under a flow of filtered nitrogen, and finally cleaned with an O_2 plasma for 3 min in a reactive ion etch chamber.

Atomic Force Microscopy. AFM of the films used for stroboSCAT was performed using an MFP-3D-BIO (Asylum Research) equipped with a BudgetSensors aluminum reflex coated silicon AFM probe Tap150AL-G-50 (Ted Pella, Inc.), and images were collected with 512 × 512 pixels at a scan rate of 0.5 lines per second in tapping mode. Film thickness was determined by comparing relative heights of the position of interest, correlated to the pump-off optical scattering image of the corresponding region, to a fiducial mark, made with a razor blade, within the same image.

AUTHOR INFORMATION

Corresponding Authors

Burak Guzelturk − *Department of Materials Science and Engineering, Stanford University, Stanford, California 94305, United States; Stanford Institute for Materials and Energy Sciences, SLAC National Accelerator Laboratory, Menlo Park, California 94025, United States;* orcid.org/0000-0003-1977-6485; Email: guzelturk@gmail.com

Aaron M. Lindenberg − *Department of Materials Science and Engineering, Stanford University, Stanford, California 94305, United States; Stanford Institute for Materials and Energy Sciences and The PULSE Institute for Ultrafast Energy Science, SLAC National Accelerator Laboratory, Menlo Park, California 94025, United States; Department of Photon Science, Stanford University and SLAC National Accelerator Laboratory, Menlo Park, California 94025, United States;* orcid.org/0000-0003-3233-7161; Email: aaronl@stanford.edu

Authors

James K. Utterback – *Department of Chemistry, University of California, Berkeley, California 94720, United States*

Igor Coropceanu – *Department of Chemistry and James Franck Institute, University of Chicago, Chicago, Illinois 60637, United States;* orcid.org/0000-0001-8057-1134

Vladislav Kamysbayev – *Department of Chemistry and James Franck Institute, University of Chicago, Chicago, Illinois 60637, United States*

Eric M. Janke – *Department of Chemistry and James Franck Institute, University of Chicago, Chicago, Illinois 60637, United States*

Marc Zajac – *Department of Materials Science and Engineering, Stanford University, Stanford, California 94305, United States*

Nuri Yazdani – *Stanford Institute for Materials and Energy Sciences, SLAC National Accelerator Laboratory, Menlo Park, California 94025, United States; Department of Information Technology and Electrical Engineering, ETH Zurich, 8092 Zurich, Switzerland*

Benjamin L. Cotts – *Department of Materials Science and Engineering, Stanford University, Stanford, California 94305, United States*

Suji Park – *Stanford Institute for Materials and Energy Sciences, SLAC National Accelerator Laboratory, Menlo Park, California 94025, United States*

Aditya Sood – *Stanford Institute for Materials and Energy Sciences, SLAC National Accelerator Laboratory, Menlo Park, California 94025, United States;* orcid.org/0000-0002-4319-666X

Ming-Fu Lin – *SLAC National Accelerator Laboratory, Menlo Park, California 94025, United States*

Alexander H. Reid – *SLAC National Accelerator Laboratory, Menlo Park, California 94025, United States*

Michael E. Kozina – *SLAC National Accelerator Laboratory, Menlo Park, California 94025, United States*

Xiaozhe Shen – *SLAC National Accelerator Laboratory, Menlo Park, California 94025, United States*

Stephen P. Weathersby – *SLAC National Accelerator Laboratory, Menlo Park, California 94025, United States*

Vanessa Wood – *Department of Information Technology and Electrical Engineering, ETH Zurich, 8092 Zurich, Switzerland;* orcid.org/0000-0001-6435-0227

Alberto Salleo – *Department of Materials Science and Engineering, Stanford University, Stanford, California 94305, United States*

Xijie Wang – *SLAC National Accelerator Laboratory, Menlo Park, California 94025, United States*

Dmitri V. Talapin – *Department of Chemistry and James Franck Institute, University of Chicago, Chicago, Illinois 60637, United States;* orcid.org/0000-0002-6414-8587

Naomi S. Ginsberg – *Department of Chemistry and Department of Physics, University of California, Berkeley, California 94720, United States; Molecular Biophysics and Integrated Bioimaging Division and Materials Sciences Division, Lawrence Berkeley National Laboratory, Berkeley, California 94720, United States; Kavli Energy NanoSciences Institute, Berkeley, California 94720, United States;* orcid.org/0000-0002-5660-3586

Notes

The authors declare no competing financial interest.

ACKNOWLEDGMENTS

The UED and stroboSCAT work is part of the "Photonics at Thermodynamic Limits" Energy Frontier Research Center funded by the U.S. Department of Energy, Office of Science, Office of Basic Energy Sciences, under Award Number DE-SC0019140. MeV-UED is operated as part of the Linac Coherent Light Source at the SLAC National Accelerator Laboratory, supported by the U.S. Department of Energy, Office of Science, Office of Basic Energy Sciences, under Contract No. DE-AC02-76SF00515. We also acknowledge support for sample preparation and characterization from the Office of Basic Energy Sciences, the U.S. Department of Energy, under Award No. DE-SC0019375. Part of this work was performed at the Stanford Nano Shared Facilities (SNSF), supported by the National Science Foundation under award ECCS-1542152. E.J. was supported by the University of Chicago Materials Research Science and Engineering Center funded by NSF under Award No. DMR-1420709. N.Y. and V.W. acknowledge funding from Swiss National Science Foundation from the Quantum Sciences and Technology NCCR. J.K.U. acknowledges the Camille and Henry Dreyfus Foundation's Postdoctoral Program in Environmental Chemistry. J.K.U. acknowledges Hannah Weaver and Jonathan Raybin for helpful discussions. M.Z., S.P., and A.S. acknowledge support from the Department of Energy, Office of Science, Basic Energy Sciences, Materials Sciences and Engineering Division, under Contract DE-AC02-76SF00515. N.S.G. and D.V.T. also acknowledge Alfred P. Sloan Research Fellowships, David and Lucile Packard Foundation Fellowships for Science and Engineering, and Camille and Henry Dreyfus Teacher-Scholar Awards.

REFERENCES

(1) Halas, N. J.; Lal, S.; Chang, W.-S.; Link, S.; Nordlander, P. Plasmons in Strongly Coupled Metallic Nanostructures. *Chem. Rev.* **2011**, *111*, 3913–3961.

(2) Pelton, M.; Aizpurua, J.; Bryant, G. Metal-Nanoparticle Plasmonics. *Laser Photonics Rev.* **2008**, *2*, 136–159.

(3) Link, S.; El-Sayed, M. A. Size and Temperature Dependence of the Plasmon Absorption of Colloidal Gold Nanoparticles. *J. Phys. Chem. B* **1999**, *103*, 4212–4217.

(4) Talapin, D. V.; Lee, J.-S.; Kovalenko, M. V.; Shevchenko, E. V. Prospects of Colloidal Nanocrystals for Electronic and Optoelectronic Applications. *Chem. Rev.* **2010**, *110*, 389–458.

(5) Murray, C. B.; Kagan, C. R.; Bawendi, M. G. Synthesis and Characterization of Monodisperse Nanocrystals and Close-Packed Nanocrystal Assemblies. *Annu. Rev. Mater. Sci.* **2000**, *30*, 545–610.

(6) Linic, S.; Christopher, P.; Ingram, D. B. Plasmonic-Metal Nanostructures for Efficient Conversion of Solar to Chemical Energy. *Nat. Mater.* **2011**, *10*, 911–921.

(7) Mukherjee, S.; Libisch, F.; Large, N.; Neumann, O.; Brown, L. V.; Cheng, J.; Lassiter, J. B.; Carter, E. A.; Nordlander, P.; Halas, N. J. Hot Electrons Do the Impossible: Plasmon-Induced Dissociation of H_2 on Au. *Nano Lett.* **2013**, *13*, 240–247.

(8) Ibáñez, M.; Luo, Z.; Genç, A.; Piveteau, L.; Ortega, S.; Cadavid, D.; Dobrozhan, O.; Liu, Y.; Nachtegaal, M.; Zebarjadi, M.; Arbiol, J.; Kovalenko, M. V.; Cabot, A. High-Performance Thermoelectric Nanocomposites from Nanocrystal Building Blocks. *Nat. Commun.* **2016**, *7*, 10766.

(9) Dreaden, E. C.; Alkilany, A. M.; Huang, X.; Murphy, C. J.; El-Sayed, M. A. The Golden Age: Gold Nanoparticles for Biomedicine. *Chem. Soc. Rev.* **2012**, *41*, 2740–2779.

(10) Huang, X.; Jain, P. K.; El-Sayed, I. H.; El-Sayed, M. A. Plasmonic Photothermal Therapy (PPTT) Using Gold Nanoparticles. *Lasers Med. Sci.* **2008**, *23*, 217–228.

(11) Brongersma, M. L.; Halas, N. J.; Nordlander, P. Plasmon-Induced Hot Carrier Science and Technology. *Nat. Nanotechnol.* **2015**, *10*, 25−34.
(12) Diroll, B. T.; Kirschner, M. S.; Guo, P.; Schaller, R. D. Optical and Physical Probing of Thermal Processes in Semiconductor and Plasmonic Nanocrystals. *Annu. Rev. Phys. Chem.* **2019**, *70*, 353−377.
(13) Hartland, G. V. Optical Studies of Dynamics in Noble Metal Nanostructures. *Chem. Rev.* **2011**, *111*, 3858−3887.
(14) Besteiro, L. V.; Yu, P.; Wang, Z.; Holleitner, A. W.; Hartland, G. V.; Wiederrecht, G. P.; Govorov, A. O. The Fast and the Furious: Ultrafast Hot Electrons in Plasmonic Metastructures. Size and Structure Matter. *Nano Today* **2019**, *27*, 120−145.
(15) Logunov, S. L.; Ahmadi, T. S.; El-Sayed, M. A.; Khoury, J. T.; Whetten, R. L. Electron Dynamics of Passivated Gold Nanocrystals Probed by Subpicosecond Transient Absorption Spectroscopy. *J. Phys. Chem. B* **1997**, *101*, 3713−3719.
(16) Hodak, J. H.; Henglein, A.; Hartland, G. V. Electron-Phonon Coupling Dynamics in Very Small (Between 2 and 8 Nm Diameter) Au Nanoparticles. *J. Chem. Phys.* **2000**, *112*, 5942−5947.
(17) Arbouet, A.; Voisin, C.; Christofilos, D.; Langot, P.; Del Fatti, N.; Vallée, F.; Lermé, J.; Celep, G.; Cottancin, E.; Gaudry, M.; Pellarin, M.; Broyer, M.; Maillard, M.; Pileni, M. P.; Treguer, M. Electron-Phonon Scattering in Metal Clusters. *Phys. Rev. Lett.* **2003**, *90*, 177401.
(18) Bauer, C.; Abid, J.-P.; Girault, H. H. Size Dependence Investigations of Hot Electron Cooling Dynamics in Metal/Adsorbates Nanoparticles. *Chem. Phys.* **2005**, *319*, 409−421.
(19) Aruda, K. O.; Tagliazucchi, M.; Sweeney, C. M.; Hannah, D. C.; Schatz, G. C.; Weiss, E. A. Identification of Parameters through Which Surface Chemistry Determines the Lifetimes of Hot Electrons in Small Au Nanoparticles. *Proc. Natl. Acad. Sci. U. S. A.* **2013**, *110*, 4212−4217.
(20) Hartland, G. V.; Besteiro, L. V.; Johns, P.; Govorov, A. O. What's so Hot about Electrons in Metal Nanoparticles? *ACS Energy Lett.* **2017**, *2*, 1641−1653.
(21) Su, M.-N.; Ciccarino, C. J.; Kumar, S.; Dongare, P. D.; Hosseini Jebeli, S. A.; Renard, D.; Zhang, Y.; Ostovar, B.; Chang, W.-S.; Nordlander, P.; Halas, N. J.; Sundararaman, R.; Narang, P.; Link, S. Ultrafast Electron Dynamics in Single Aluminum Nanostructures. *Nano Lett.* **2019**, *19*, 3091−3097.
(22) Saavedra, J. R. M.; Asenjo-Garcia, A.; García de Abajo, F. J. Hot-Electron Dynamics and Thermalization in Small Metallic Nanoparticles. *ACS Photonics* **2016**, *3*, 1637−1646.
(23) Wilson, O. M.; Hu, X.; Cahill, D. G.; Braun, P. V. Colloidal Metal Particles as Probes of Nanoscale Thermal Transport in Fluids. *Phys. Rev. B: Condens. Matter Mater. Phys.* **2002**, *66*, 224301.
(24) Juvé, V.; Scardamaglia, M.; Maioli, P.; Crut, A.; Merabia, S.; Joly, L.; Del Fatti, N.; Vallée, F. Cooling Dynamics and Thermal Interface Resistance of Glass-Embedded Metal Nanoparticles. *Phys. Rev. B: Condens. Matter Mater. Phys.* **2009**, *80*, 195406.
(25) Park, J.; Huang, J.; Wang, W.; Murphy, C. J.; Cahill, D. G. Heat Transport between Au Nanorods, Surrounding Liquids, and Solid Supports. *J. Phys. Chem. C* **2012**, *116*, 26335−26341.
(26) Nguyen, S. C.; Zhang, Q.; Manthiram, K.; Ye, X.; Lomont, J. P.; Harris, C. B.; Weller, H.; Alivisatos, A. P. Study of Heat Transfer Dynamics from Gold Nanorods to the Environment *via* Time-Resolved Infrared Spectroscopy. *ACS Nano* **2016**, *10*, 2144−2151.
(27) Wu, X.; Ni, Y.; Zhu, J.; Burrows, N. D.; Murphy, C. J.; Dumitrica, T.; Wang, X. Thermal Transport across Surfactant Layers on Gold Nanorods in Aqueous Solution. *ACS Appl. Mater. Interfaces* **2016**, *8*, 10581−10589.
(28) Hu, M.; Hartland, G. V. Heat Dissipation for Au Particles in Aqueous Solution: Relaxation Time *versus* Size. *J. Phys. Chem. B* **2003**, *107*, 1284−1284.
(29) Buzzi, M.; Först, M.; Mankowsky, R.; Cavalleri, A. Probing Dynamics in Quantum Materials with Femtosecond X-Rays. *Nat. Rev. Mater.* **2018**, *3*, 299−311.
(30) Clark, J. N.; Beitra, L.; Xiong, G.; Higginbotham, A.; Fritz, D. M.; Lemke, H. T.; Zhu, D.; Chollet, M.; Williams, G. J.; Messerschmidt, M.; Abbey, B.; Harder, R. J.; Korsunsky, A. M.; Wark, J. S.; Robinson, I. K. Ultrafast Three-Dimensional Imaging of Lattice Dynamics in Individual Gold Nanocrystals. *Science* **2013**, *341*, 56−59.
(31) Flannigan, D. J.; Lindenberg, A. M. Atomic-Scale Imaging of Ultrafast Materials Dynamics. *MRS Bull.* **2018**, *43*, 485−490.
(32) Wu, X.; Tan, L. Z.; Shen, X.; Hu, T.; Miyata, K.; Tuan Trinh, M.; Li, R.; Coffee, R.; Liu, S.; Egger, D. A.; Makasyuk, I.; Zheng, Q.; Fry, A.; Robinson, J. S.; Smith, M. D.; Guzelturk, B.; Karunadasa, H. I.; Wang, X.; Zhu, X.; Kronik, L.; et al. Light-Induced Picosecond Rotational Disordering of the Inorganic Sublattice in Hybrid Perovskites. *Sci. Adv.*, **2017**, *3*, e1602388.
(33) Vasileiadis, T.; Waldecker, L.; Foster, D.; Da Silva, A.; Zahn, D.; Bertoni, R.; Palmer, R. E.; Ernstorfer, R. Ultrafast Heat Flow in Heterostructures of Au Nanoclusters on Thin Films: Atomic Disorder Induced by Hot Electrons. *ACS Nano* **2018**, *12*, 7710−7720.
(34) Vanacore, G. M.; Hu, J.; Liang, W.; Bietti, S.; Sanguinetti, S.; Zewail, A. H. Diffraction of Quantum Dots Reveals Nanoscale Ultrafast Energy Localization. *Nano Lett.* **2014**, *14*, 6148−6154.
(35) Mancini, G. F.; Latychevskaia, T.; Pennacchio, F.; Reguera, J.; Stellacci, F.; Carbone, F. Order/Disorder Dynamics in a Dodecanethiol-Capped Gold Nanoparticles Supracrystal by Small-Angle Ultrafast Electron Diffraction. *Nano Lett.* **2016**, *16*, 2705−2713.
(36) Link, S.; Hathcock, D. J.; Nikoobakht, B.; El-Sayed, M. A. Medium Effect on the Electron Cooling Dynamics in Gold Nanorods and Truncated Tetrahedra. *Adv. Mater.* **2003**, *15*, 393−396.
(37) Liebsch, A. Surface-Plasmon Dispersion and Size Dependence of Mie Resonance: Silver *versus* Simple Metals. *Phys. Rev. B: Condens. Matter Mater. Phys.* **1993**, *48*, 11317−11328.
(38) Voisin, C.; Del Fatti, N.; Christofilos, D.; Vallée, F. Ultrafast Electron Dynamics and Optical Nonlinearities in Metal Nanoparticles. *J. Phys. Chem. B* **2001**, *105*, 2264−2280.
(39) Ong, W.-L.; Rupich, S. M.; Talapin, D. V.; McGaughey, A. J. H.; Malen, J. A. Surface Chemistry Mediates Thermal Transport in Three-Dimensional Nanocrystal Arrays. *Nat. Mater.* **2013**, *12*, 410−415.
(40) Liu, M.; Ma, Y.; Wang, R. Y. Modifying Thermal Transport in Colloidal Nanocrystal Solids with Surface Chemistry. *ACS Nano* **2015**, *9*, 12079−12087.
(41) Wu, K.; Chen, J.; McBride, J. R.; Lian, T. Efficient Hot-Electron Transfer by a Plasmon-Induced Interfacial Charge-Transfer Transition. *Science* **2015**, *349*, 632−635.
(42) Zhang, Y.; He, S.; Guo, W.; Hu, Y.; Huang, J.; Mulcahy, J. R.; Wei, W. D. Surface-Plasmon-Driven Hot Electron Photochemistry. *Chem. Rev.* **2018**, *118*, 2927−2954.
(43) Aslam, U.; Rao, V. G.; Chavez, S.; Linic, S. Catalytic Conversion of Solar to Chemical Energy on Plasmonic Metal Nanostructures. *Nat. Catal.* **2018**, *1*, 656−665.
(44) Huang, J.; Park, J.; Wang, W.; Murphy, C. J.; Cahill, D. G. Ultrafast Thermal Analysis of Surface Functionalized Gold Nanorods in Aqueous Solution. *ACS Nano* **2013**, *7*, 589−597.
(45) Diroll, B. T.; Guo, P.; Schaller, R. D. Heat Transfer at Hybrid Interfaces: Interfacial Ligand-To-Nanocrystal Heating Monitored with Infrared Pump. *Nano Lett.* **2018**, *18*, 7863−7869.
(46) Losego, M. D.; Grady, M. E.; Sottos, N. R.; Cahill, D. G.; Braun, P. V. Effects of Chemical Bonding on Heat Transport across Interfaces. *Nat. Mater.* **2012**, *11*, 502−506.
(47) Weathersby, S. P.; Brown, G.; Centurion, M.; Chase, T. F.; Coffee, R.; Corbett, J.; Eichner, J. P.; Frisch, J. C.; Fry, A. R.; Gühr, M.; Hartmann, N.; Hast, C.; Hettel, R.; Jobe, R. K.; Jongewaard, E. N.; Lewandowski, J. R.; Li, R. K.; Lindenberg, A. M.; Makasyuk, I.; May, J. E.; et al. Mega-Electron-Volt Ultrafast Electron Diffraction at SLAC National Accelerator Laboratory. *Rev. Sci. Instrum.* **2015**, *86*, No. 073702.
(48) Cremons, D. R.; Flannigan, D. J. Direct *In Situ* Thermometry: Variations in Reciprocal-Lattice Vectors and Challenges with the Debye−Waller Effect. *Ultramicroscopy* **2016**, *161*, 10−16.
(49) Banerjee, S.; Liu, C.-H.; Lee, J. D.; Kovyakh, A.; Grasmik, V.; Prymak, O.; Koenigsmann, C.; Liu, H.; Wang, L.; Abeykoon, A. M.

M.; Wong, S. S.; Epple, M.; Murray, C. B.; Billinge, S. J. L. Improved Models for Metallic Nanoparticle Cores from Atomic Pair Distribution Function (PDF) Analysis. *J. Phys. Chem. C* **2018**, *122*, 29498−29506.
(50) Sokolowski-Tinten, K.; Shen, X.; Zheng, Q.; Chase, T.; Coffee, R.; Jerman, M.; Li, R. K.; Ligges, M.; Makasyuk, I.; Mo, M.; Reid, A. H.; Rethfeld, B.; Vecchione, T.; Weathersby, S. P.; Dürr, H. A.; Wang, X. J. Electron-Lattice Energy Relaxation in Laser-Excited Thin-Film Au-Insulator Heterostructures Studied by Ultrafast MeV Electron Diffraction. *Struct. Dyn.* **2017**, *4*, No. 054501.
(51) Groeneveld, R. H. M.; Sprik, R.; Lagendijk, A. Femtosecond Spectroscopy of Electron-Electron and Electron-Phonon Energy Relaxation in Ag and Au. *Phys. Rev. B: Condens. Matter Mater. Phys.* **1995**, *51*, 11433−11445.
(52) Lin, Z.; Zhigilei, L. V.; Celli, V. Electron-Phonon Coupling and Electron Heat Capacity of Metals under Conditions of Strong Electron-Phonon Nonequilibrium. *Phys. Rev. B: Condens. Matter Mater. Phys.* **2008**, *77*, No. 075133.
(53) Del Fatti, N.; Voisin, C.; Achermann, M.; Tzortzakis, S.; Christofilos, D.; Vallée, F. Nonequilibrium Electron Dynamics in Noble Metals. *Phys. Rev. B: Condens. Matter Mater. Phys.* **2000**, *61*, 16956−16966.
(54) Schulz-Dobrick, M.; Vijaya-Sarathy, K.; Jansen, M. Surfactant-Free Synthesis and Functionalization of Gold Nanoparticles. *J. Am. Chem. Soc.* **2005**, *127*, 12816−12817.
(55) Leff, D. V.; Brandt, L.; Heath, J. R. Synthesis and Characterization of Hydrophobic, Organically-Soluble Gold Nanocrystals Functionalized with Primary Amines. *Langmuir* **1996**, *12*, 4723−4730.
(56) Govorov, A. O.; Zhang, H.; Demir, H. V.; Gun'ko, Y. K. Photogeneration of Hot Plasmonic Electrons with Metal Nanocrystals: Quantum Description and Potential Applications. *Nano Today* **2014**, *9*, 85−101.
(57) Zhao, J.; Nguyen, S. C.; Ye, R.; Ye, B.; Weller, H.; Somorjai, G. A.; Alivisatos, A. P.; Toste, F. D. A Comparison of Photocatalytic Activities of Gold Nanoparticles Following Plasmonic and Interband Excitation and a Strategy for Harnessing Interband Hot Carriers for Solution Phase Photocatalysis. *ACS Cent. Sci.* **2017**, *3*, 482−488.
(58) Govorov, A. O.; Zhang, W.; Skeini, T.; Richardson, H.; Lee, J.; Kotov, N. A. Gold Nanoparticle Ensembles as Heaters and Actuators: Melting and Collective Plasmon Resonances. *Nanoscale Res. Lett.* **2006**, *1*, 84−90.
(59) Zheng, Q.; Shen, X.; Sokolowski-Tinten, K.; Li, R. K.; Chen, Z.; Mo, M. Z.; Wang, Z. L.; Weathersby, S. P.; Yang, J.; Chen, M. W.; Wang, X. J. Dynamics of Electron−Phonon Coupling in Bicontinuous Nanoporous Gold. *J. Phys. Chem. C* **2018**, *122*, 16368−16373.
(60) Ekardt, W. Work Function of Small Metal Particles: Self-Consistent Spherical Jellium-Background Model. *Phys. Rev. B: Condens. Matter Mater. Phys.* **1984**, *29*, 1558−1564.
(61) Harutyunyan, H.; Martinson, A. B. F.; Rosenmann, D.; Khorashad, L. K.; Besteiro, L. V.; Govorov, A. O.; Wiederrecht, G. P. Anomalous Ultrafast Dynamics of Hot Plasmonic Electrons in Nanostructures with Hot Spots. *Nat. Nanotechnol.* **2015**, *10*, 770−774.
(62) Magnozzi, M.; Proietti Zaccaria, R.; Catone, D.; O'Keeffe, P.; Paladini, A.; Toschi, F.; Alabastri, A.; Canepa, M.; Bisio, F. Interband Transitions Are More Efficient Than Plasmonic Excitation in the Ultrafast Melting of Electromagnetically Coupled Au Nanoparticles. *J. Phys. Chem. C* **2019**, *123*, 16943−16950.
(63) Foerster, B.; Joplin, A.; Kaefer, K.; Celiksoy, S.; Link, S.; Sönnichsen, C. Chemical Interface Damping Depends on Electrons Reaching the Surface. *ACS Nano* **2017**, *11*, 2886−2893.
(64) Shirhatti, P. R.; Rahinov, I.; Golibrzuch, K.; Werdecker, J.; Geweke, J.; Altschäffel, J.; Kumar, S.; Auerbach, D. J.; Bartels, C.; Wodtke, A. M. Observation of the Adsorption and Desorption of Vibrationally Excited Molecules on a Metal Surface. *Nat. Chem.* **2018**, *10*, 592−598.
(65) Zhou, L.; Swearer, D. F.; Zhang, C.; Robatjazi, H.; Zhao, H.; Henderson, L.; Dong, L.; Christopher, P.; Carter, E. A.; Nordlander, P.; Halas, N. J. Quantifying Hot Carrier and Thermal Contributions in Plasmonic Photocatalysis. *Science* **2018**, *362*, 69−72.
(66) Abbas, M. A.; Kamat, P. V.; Bang, J. H. Thiolated Gold Nanoclusters for Light Energy Conversion. *ACS Energy Lett.* **2018**, *3*, 840−854.
(67) Wan, X.-K.; Wang, J.-Q.; Nan, Z.-A.; Wang, Q.-M. Ligand Effects in Catalysis by Atomically Precise Gold Nanoclusters. *Sci. Adv.* **2017**, *3*, No. e1701823.
(68) Ong, W.-L.; Majumdar, S.; Malen, J. A.; McGaughey, A. J. H. Coupling of Organic and Inorganic Vibrational States and Their Thermal Transport in Nanocrystal Arrays. *J. Phys. Chem. C* **2014**, *118*, 7288−7295.
(69) Stocker, K. M.; Neidhart, S. M.; Gezelter, J. D. Interfacial Thermal Conductance of Thiolate-Protected Gold Nanospheres. *J. Appl. Phys.* **2016**, *119*, No. 025106.
(70) Delor, M.; Weaver, H. L.; Yu, Q.; Ginsberg, N. S. Imaging Material Functionality through Three-Dimensional Nanoscale Tracking of Energy Flow. *Nat. Mater.* **2020**, *19*, 56−62.
(71) Picard, S.; Burns, D. T.; Roger, P. Determination of the Specific Heat Capacity of a Graphite Sample Using Absolute and Differential Methods. *Metrologia* **2007**, *44*, 294−302.
(72) Koontz, E. Thermal Analysis of Glass. In *Springer Handbook of Glass*; Musgraves, J. D., Hu, J. C., Eds.; Springer Handbooks: Cham, 2019; pp 853−878.
(73) Bouchaud, J.-P.; Georges, A. Anomalous Diffusion in Disordered Media: Statistical Mechanisms, Models and Physical Applications. *Phys. Rep.* **1990**, *195*, 127−293.
(74) Li, B.; Wang, J. Anomalous Heat Conduction and Anomalous Diffusion in One-Dimensional Systems. *Phys. Rev. Lett.* **2003**, *91*, No. 044301.
(75) Schneider, C. A.; Rasband, W. S.; Eliceiri, K. W. NIH Image to ImageJ: 25 Years of Image Analysis. *Nat. Methods* **2012**, *9*, 671−675.
(76) Schindelin, J.; Arganda-Carreras, I.; Frise, E.; Kaynig, V.; Longair, M.; Pietzsch, T.; Preibisch, S.; Rueden, C.; Saalfeld, S.; Schmid, B.; Tinevez, J.-Y.; White, D. J.; Hartenstein, V.; Eliceiri, K.; Tomancak, P.; Cardona, A. Fiji: An Open-Source Platform for Biological-Image Analysis. *Nat. Methods* **2012**, *9*, 676−682.
(77) Yang, Y.; Wang, B.; Shen, X.; Yao, L.; Wang, L.; Chen, X.; Xie, S.; Li, T.; Hu, J.; Yang, D.; Dong, A. Scalable Assembly of Crystalline Binary Nanocrystal Superparticles and Their Enhanced Magnetic and Electrochemical Properties. *J. Am. Chem. Soc.* **2018**, *140*, 15038−15047.